Supplementary Information

Viable post-electrode-engineering for the complete integrity of large-volume-change lithium-ion battery anodes

Jihun Kim [a, b], Jiyoung Ma [b], Hocheol Yoon [a], Junsung Jang [c], Seokho Suh [a], Hyeonghun Park [a], Jeonghwan Song, [b] Jin Hyeok Kim [c], Junsu Park [d], Jung-Je Woo [b,], and Hyeong-Jin Kim [a,]**

[a] Graduate School of Energy Convergence, Gwangju Institute of Science and Technology

123 Cheomdangwagi-ro, Gwangju 61005, Republic of Korea

[b] Gwangju Bio/Energy R&D Center, Korea Institute of Energy Research (KIER)

270-25 Samso-ro, Gwangju, 61003, Republic of Korea

[c] Optoelectronic Convergence Research Center, Department of Materials Science and Engineering, Chonnam National University, 77 Yongong-ro, Gwangju 61186, Republic of Korea

[d] Ground Technology Research Institute, Agency for Defense Development P.O. Box 35, Daejeon 34186, Republic of Korea

Corresponding E-mail: hjkimc@gist.ac.kr (H. -J. Kim), wooj@kier.re.kr (J. -J. Woo)

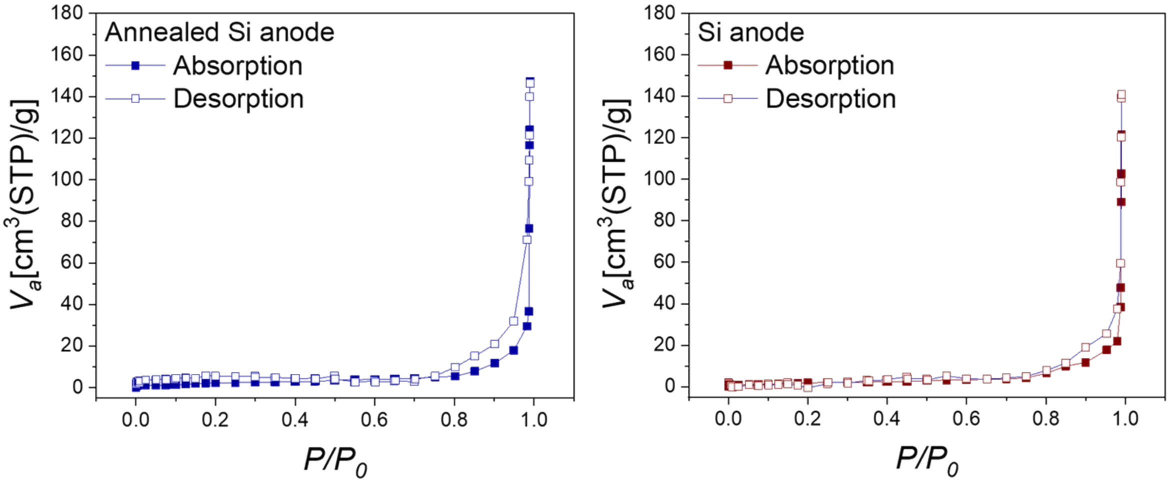

Figure S1. Adsorption-desorption isotherm curves for the annealed Si and bare Si electrodes.

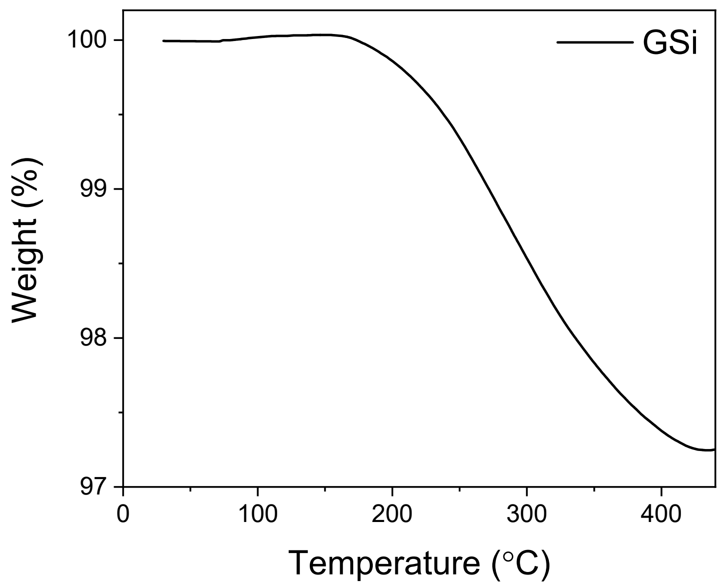

Figure S2. TGA result for GSi to measure the carbon content added by rGO coating.

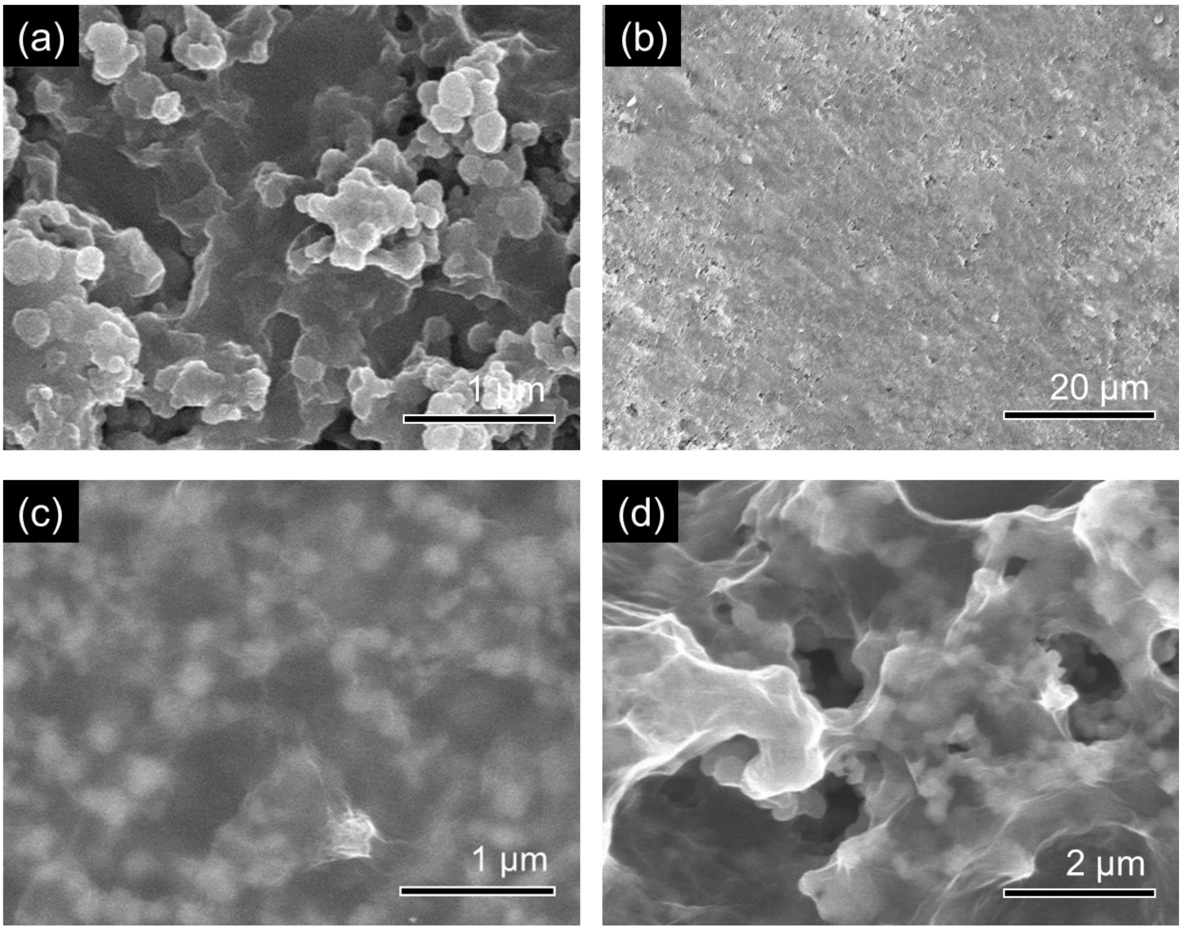

Figure S3. Surface FE-SEM image for (a)/(b) Gsi and, (b)/(c) rGO seed layer coated on the GSi. Across the opaque view of the rGO seed layer, Si particles can be confirmed.

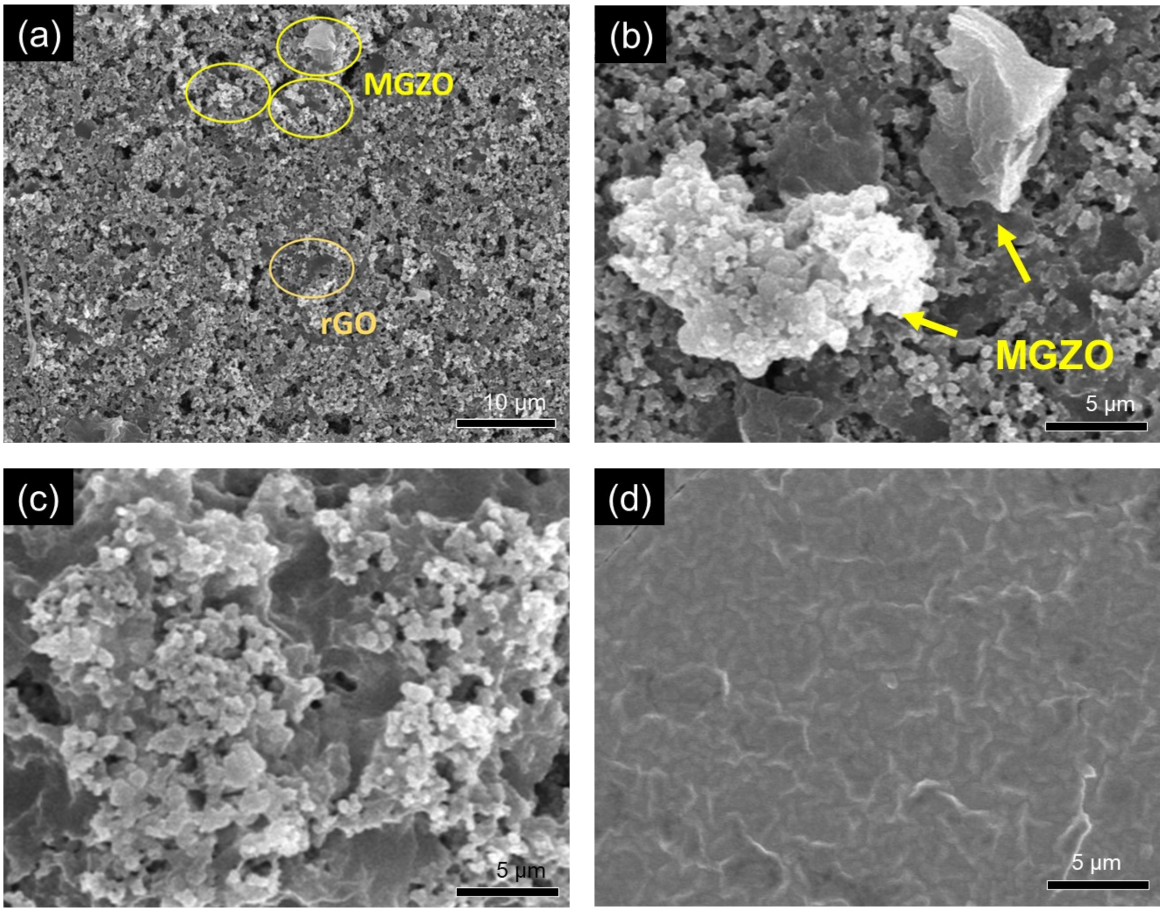

Figure S4. (a)-(c) Surface FE-SEM image for deposition of MGZO MO on the GSi without the rGO seed layer. (d) Surface of MGZO film that is successfully deposited on the GSi with rGO seed layer. The MGZO film cannot show two-dimensional growth on the surface without a seed layer. Island-type growth for MGZO did not successfully settle during the sputtering deposition. The growth site was not found, and it had an amorphous form and could not be grown as a film on the GSi surface. The rGO does not need any post-removal step and can be easily applied using a facile spin coating method, thus it is a suitable seed layer for the subsequent deposition of the MGZO metal oxide layers.

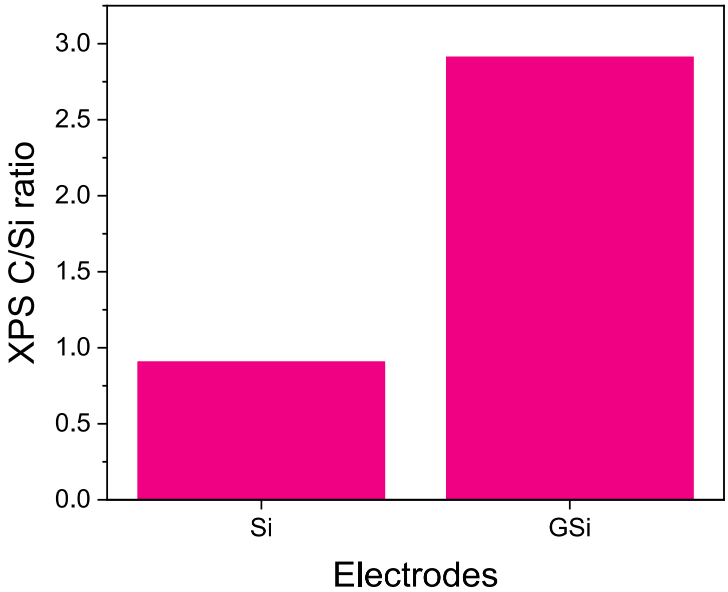

Figure S5. XPS carbon/Si ratio for the Si and GSi electrodes.

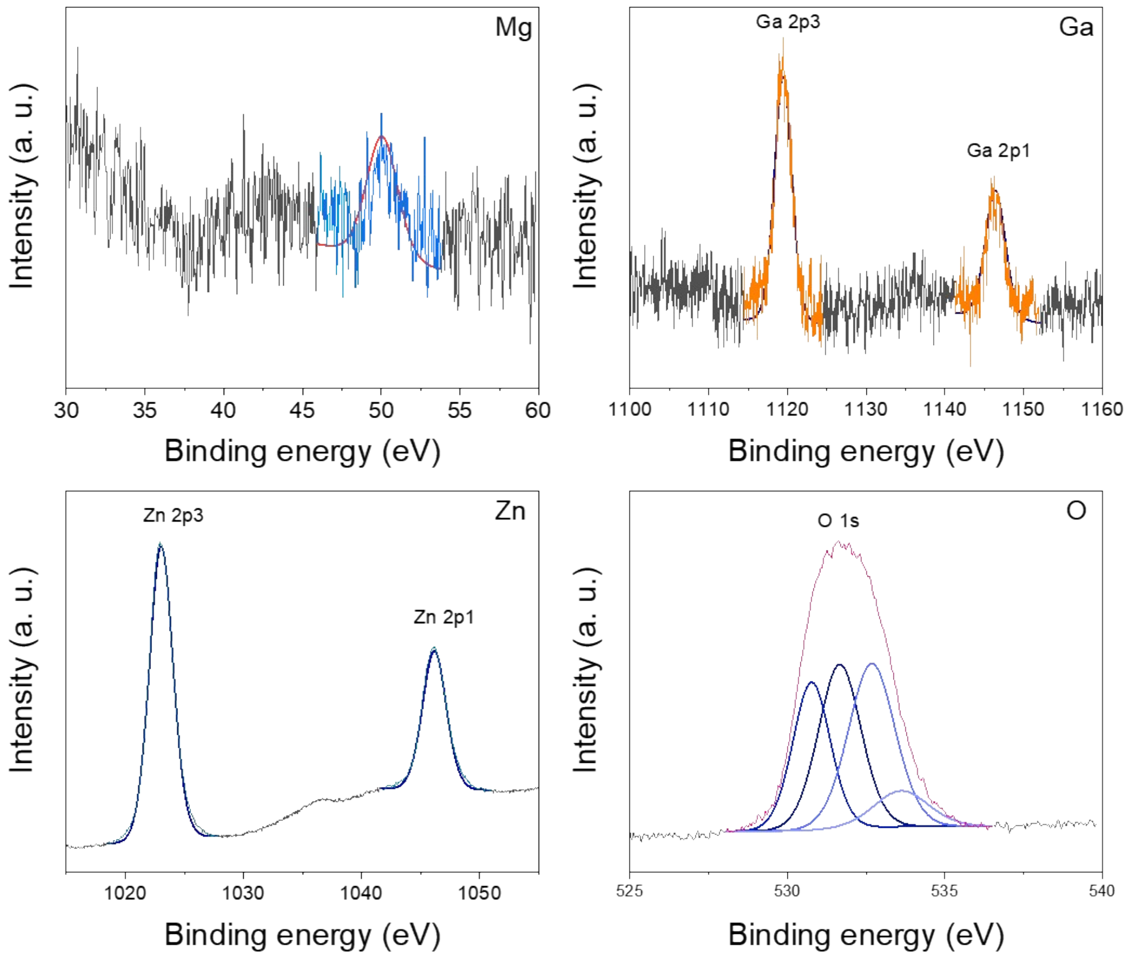

Figure S6. XPS spectra of Mg, Ga, Zn and O in the GSi-MGZO.

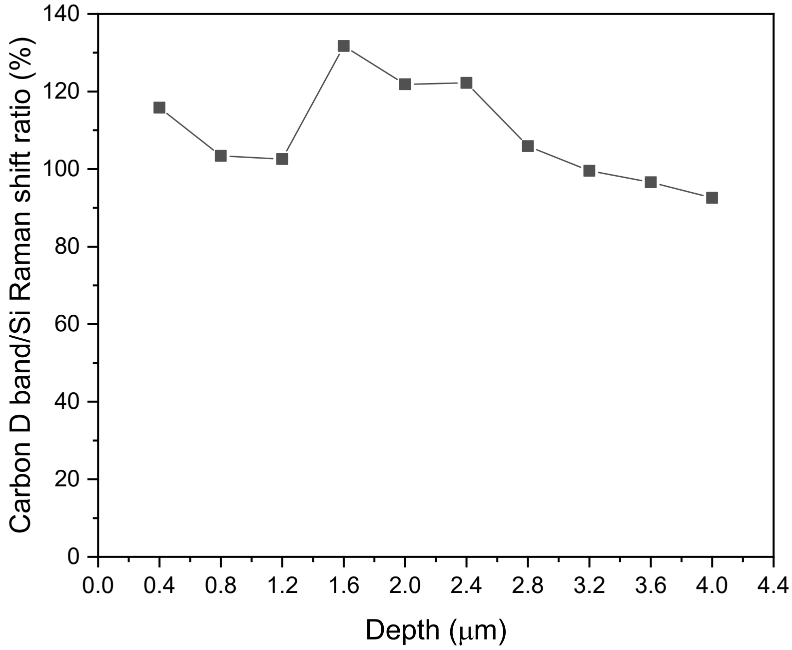

Figure S7. Raman shift ratio of carbon and Si in conductive carbon free-GSi depending on depth.

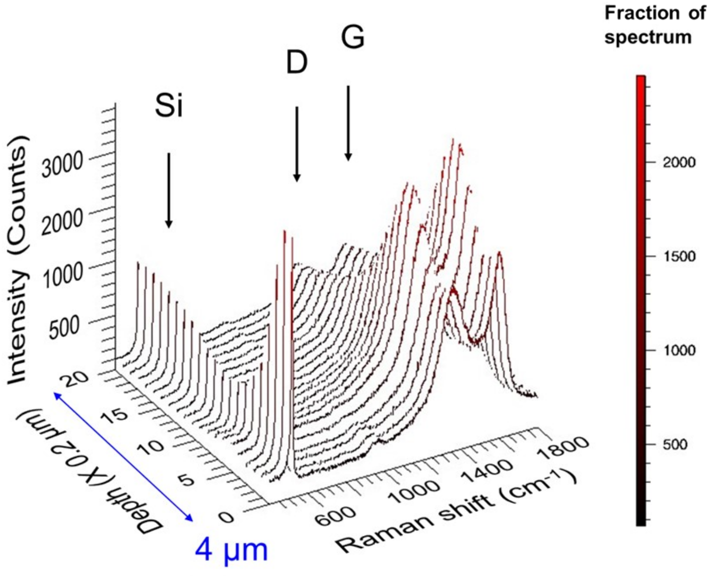

Figure S8. Three-dimensional Raman elemental depth profiling for GSi electrode.

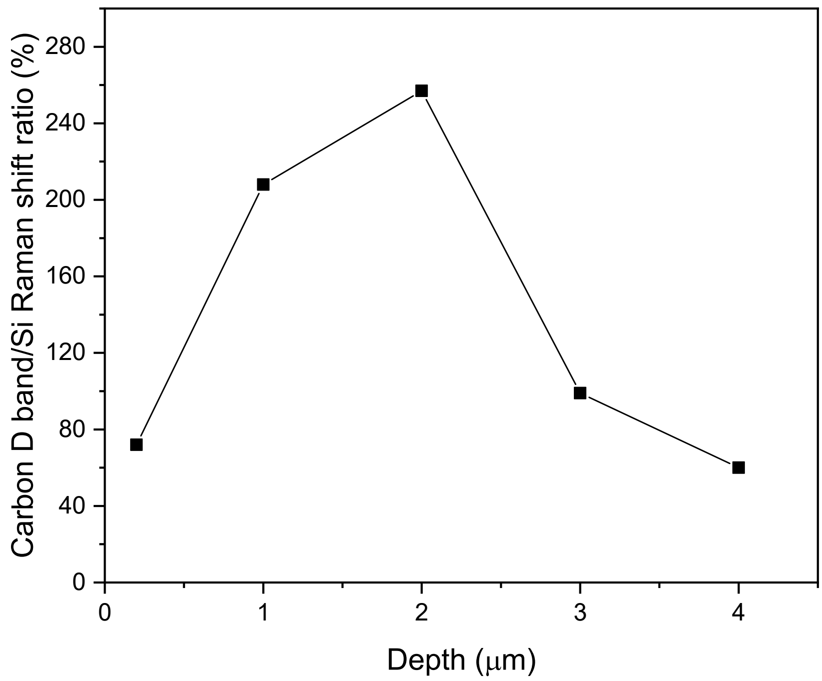

Figure S9. Raman shifts ratio of carbon and Si in the GSi electrode depending on depth.

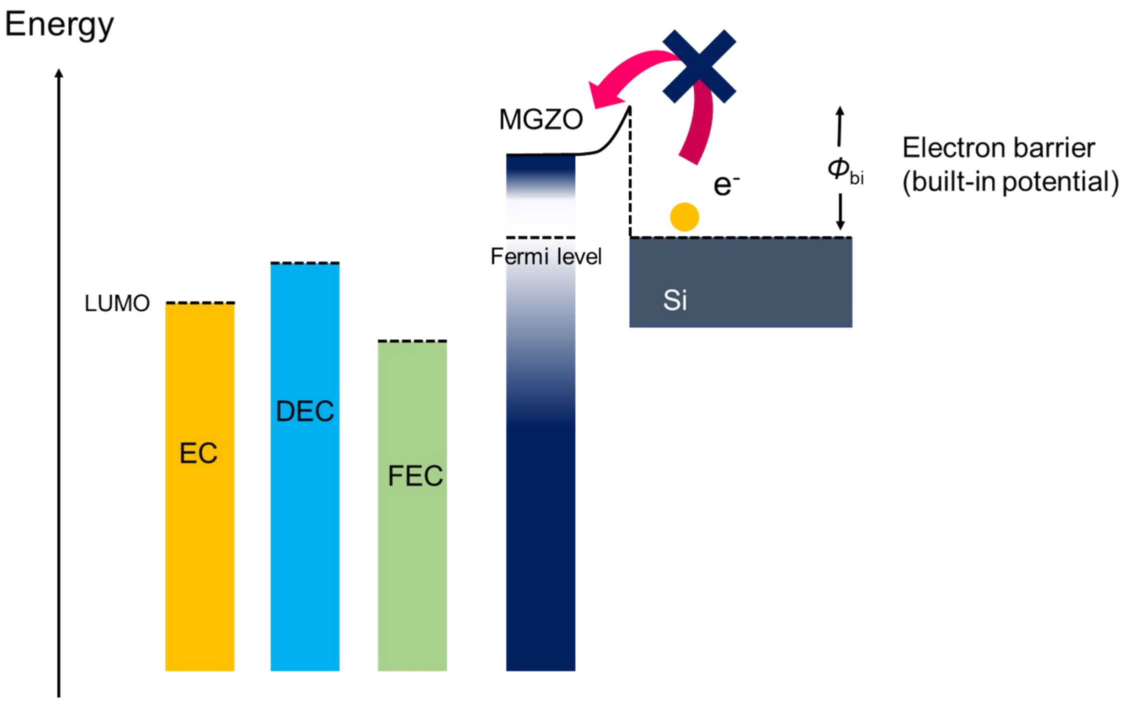

Figure S10. Schematic of energy diagram for MGZO with Si anode depicting the electron barrier.

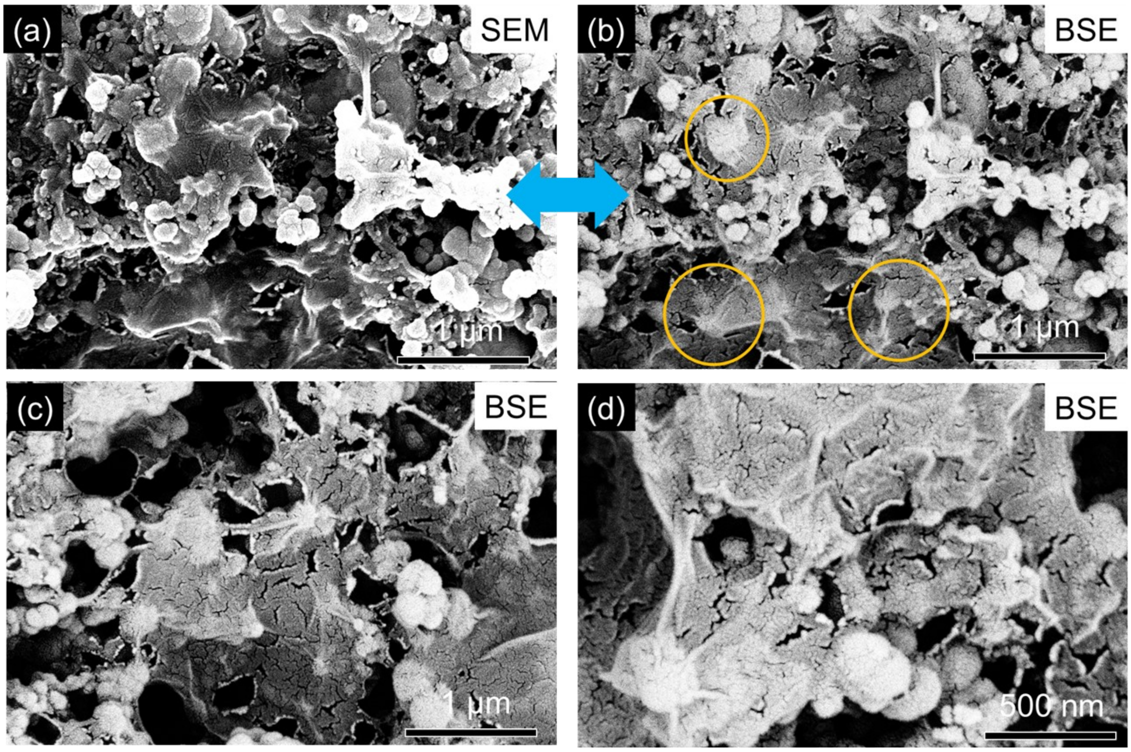

Figure S11. (a) SEM and (b)-(d) BSE images of the GSi. BSE image enable comfirming the hazy Si particles in the rGO web by whitish image (See circles in Figure S 10b).

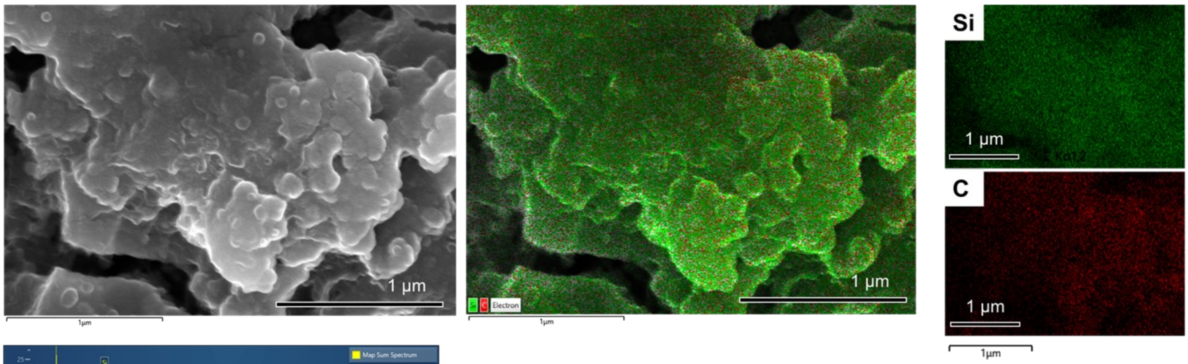

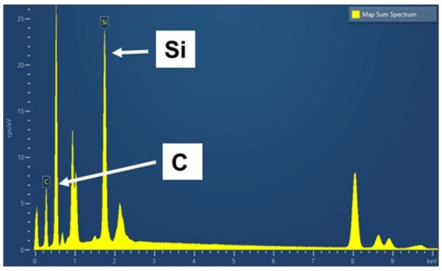

Map Sum Spectrum				
Element	Line Type	Apparent Concentration	k Ratio	Wt%
C	K series	7.80	0.07798	76.24
Si	K series	15.97	0.12654	23.76
Total:				100.00

Figure S12. EDS elemental mapping results for the electrochemically aggregated Si-rGO bulk.

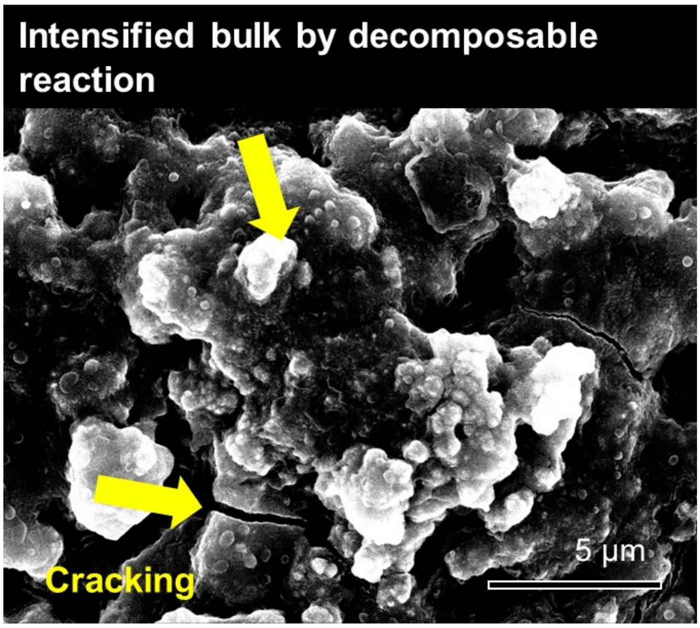

Figure S13. Surface FE-SEM image for GSi after 200 cycles.

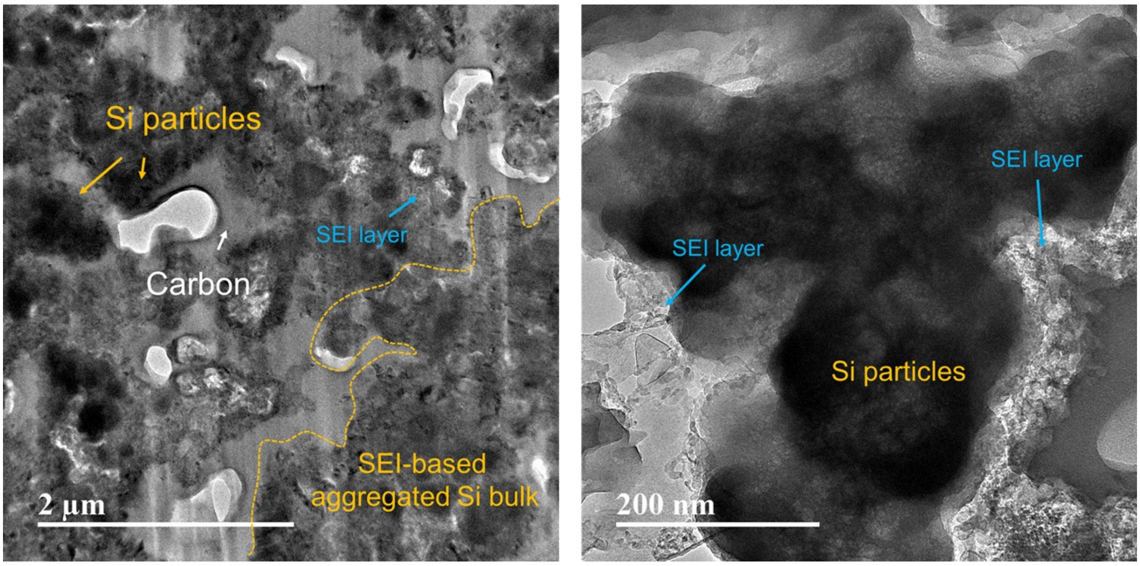

Figure S14. TEM images for the cycled bare Si electrode.

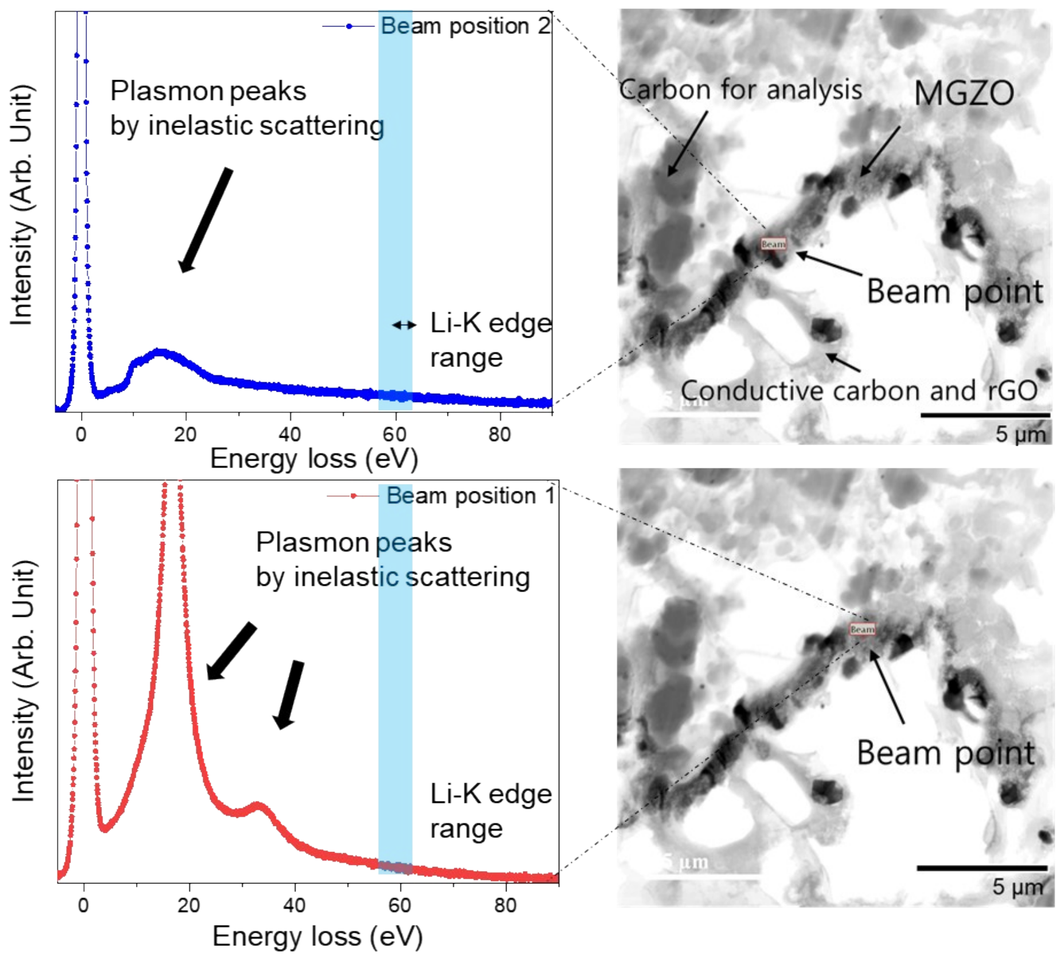

Figure S15. EELS spectra and STEM images for the fully-lithiated GSi-MGZO electrode. The measurement was conducted depending on the beam positions on the MGZO layer.

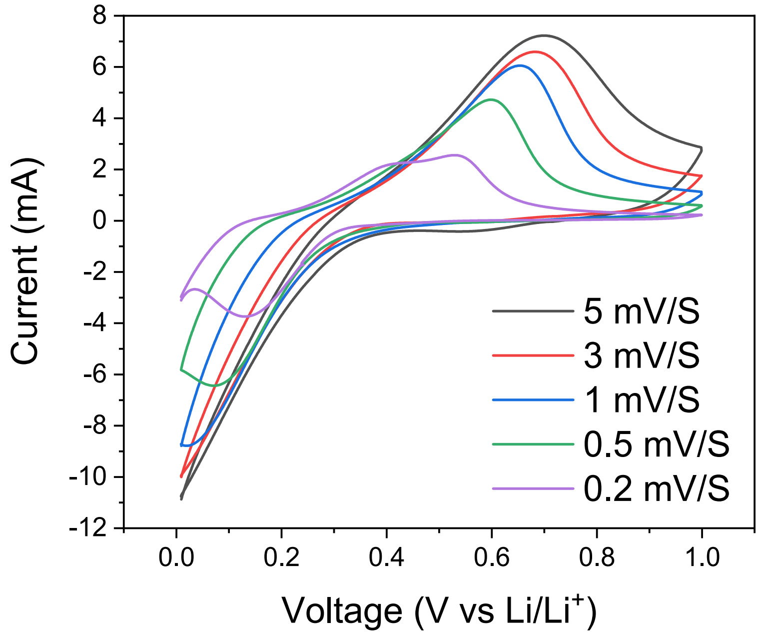

Figure S16. CV curves for the GSi-MGZO electrode according to the scan rate.

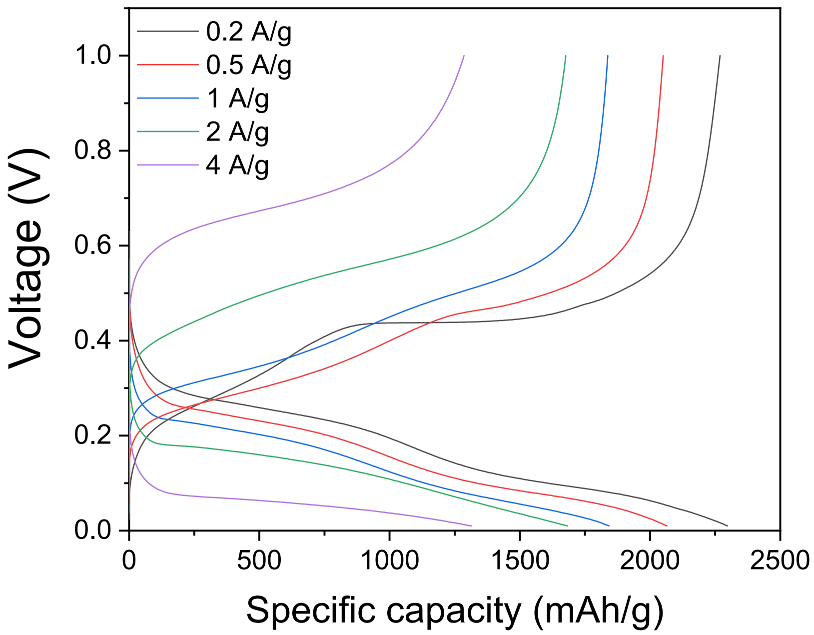

Figure S17. Galvanostatic charge/discharge curves for GSi-MGZO according to the current density.

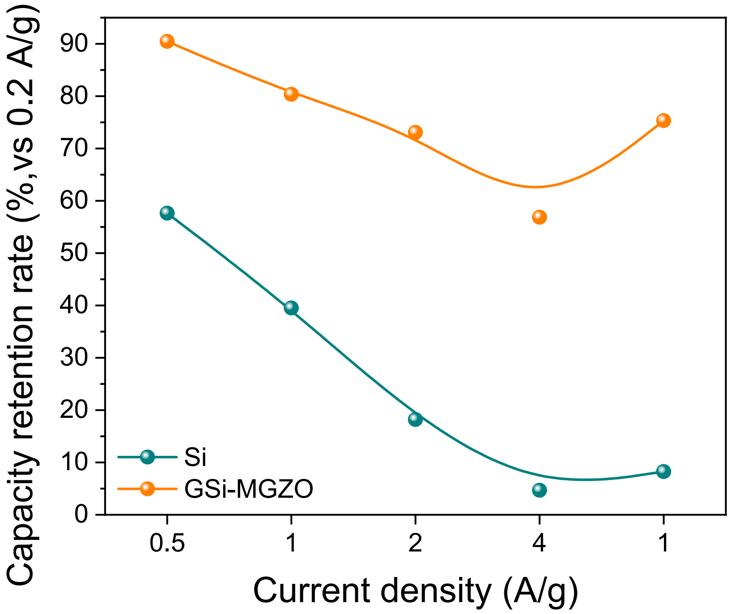

Figure S18. Capacity retention rate (vs 0.2 A g^{-1}) for the Si and the GSi-MGZO electrodes as a function of the current density. At a high current density up to 4 A g^{-1}, the GSi-MGZO electrode shows an excellent capacity retention. At a current density of up to 2 A g^{-1}, the capacity retention is more than 70%. However, in the case of the Si electrode, the capacity retention rate rapidly decreases to 4% at 4 A g^{-1}, and there is an unfavorable capacity retention of 18% at a current density of 2 A g^{-1}. The GSi-MGZO electrode exhibits a similar capacity even at 1 A g^{-1} after testing at a current density of 4 A g^{-1}, whereas the Si electrode exhibits a decreased capacity at 1 A g^{-1} after the test at a high density of 4 A g^{-1}.

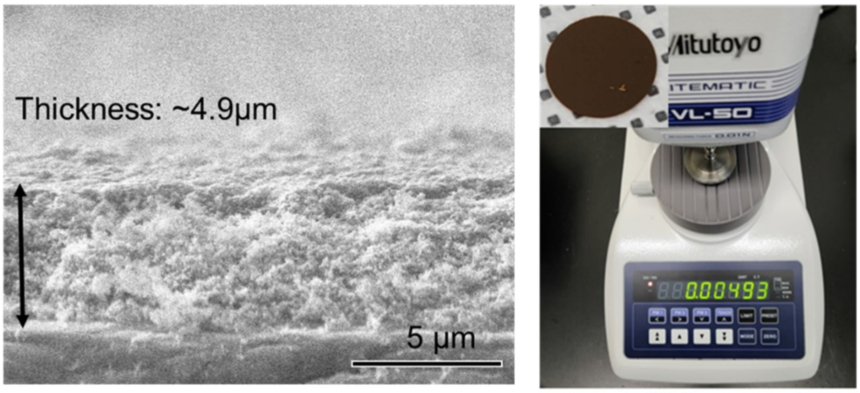

Measured thickness: ~4.93 μm

Area: 0.785 cm^2

Thickness : 4.9 μm

Mass: 0.43 mg

$$\text{Volumetric capacity} = \frac{Specific\ capacity\ \left(mAh\ g^{-1}\right) \times Mass\ (g)}{Area\ (cm^2) \times Thickness\ (cm)}$$

Figure S19. Information related to volumetric capacity for GSi-MGZO.

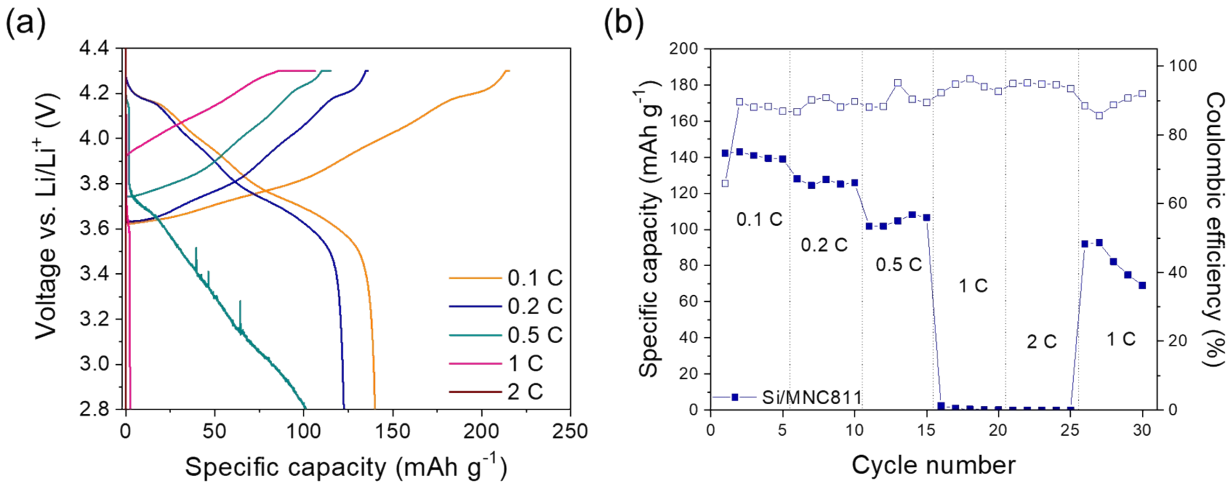

Figure S20. (a) Initial galvanostatic charge/discharge curves for the Si/NMC811 full cell with variation in the current densities from 0.1 to 2 C. (b) Rate performance of the Si/NMC811 full cell with variation in the current densities from 0.1 to 2 C.

Table S1. Details derived from BET plots for the annealed and bare Si electrodes.

	Si	Annealed Si
Standard volume (cm^3)	34.163	34.163
Dead volume (cm^3)	38.678	38.727
BET surface area(m^2/g)	6.47	7.76
Total pore volume [p/p_0=0.990] (cm^3/g)	0.170	0.211
Mean pore diameter (nm)	105.16	109.02
Maximum pore volume [cm^3 (STP)/g]	1.486	1.782

Table S2. Representative literature data for volumetric capacity

Materials	C-rate	Volumetric capacity	Reference
Carbon coated Si nanowires	0.2 C	~2500 mAh/cm^3	1
Shell coating nanoparticles	0.05 C	2041 mAh/cm^3	2
Carbon-garphene template	0.5 C	1807 mAh/cm^3	3
SnO_2@Si nanospheres	0.075 C	1615 mAh/cm^3	4
Hierarchical Si@TiO_2@C	0.025 C	1174 mAh/cm^3	5
Porous Si microparticles	0.065 C	1075 mAh/cm^3	6
Carbon coated porous Si	0.05 C	1003 mAh/cm^3	7
GSi-MGZO	0.025 C/ 0.25 C	2766/2710 mAh/cm^3	This work

1. Wang, B.; Ryu, J.; Choi, S.; Zhang, X.; Pribat, D.; Li, X.; Zhi, L.; Park, S.; Ruoff, R. S., Ultrafast-Charging Silicon-Based Coral-Like Network Anodes for Lithium-Ion Batteries with High Energy and Power Densities. *ACS Nano* **2019,** *13* (2), 2307-2315.
2. Wang, J.; Liao, L.; Li, Y.; Zhao, J.; Shi, F.; Yan, K.; Pei, A.; Chen, G.; Li, G.; Lu, Z.; Cui, Y., Shell-Protective Secondary Silicon Nanostructures as Pressure-Resistant High-Volumetric-Capacity Anodes for Lithium-Ion Batteries. *Nano Lett.* **2018,** *18* (11), 7060-7065.
3. Zhou, M.; Li, X.; Wang, B.; Zhang, Y.; Ning, J.; Xiao, Z.; Zhang, X.; Chang, Y.; Zhi, L., High-Performance Silicon Battery Anodes Enabled by Engineering Graphene Assemblies. *Nano Lett.* **2015,** *15* (9), 6222-6228.
4. Shi, J.; Zu, L.; Gao, H.; Hu, G.; Zhang, Q., Silicon-Based Self-Assemblies for High Volumetric Capacity Li-Ion Batteries via Effective Stress Management. *Adv. Funct. Mater.* **2020,** *30* (35), 2002980.
5. Lu, Z.; Liu, N.; Lee, H.-W.; Zhao, J.; Li, W.; Li, Y.; Cui, Y., Nonfilling Carbon Coating of Porous Silicon Micrometer-Sized Particles for High-Performance Lithium Battery Anodes. *ACS Nano* **2015,** *9* (3), 2540-2547.
6. Ma, T.; Yu, X.; Li, H.; Zhang, W.; Cheng, X.; Zhu, W.; Qiu, X., High Volumetric Capacity of Hollow Structured SnO_2@Si Nanospheres for Lithium-Ion Batteries. *Nano Lett.* **2017,** *17* (6), 3959-3964.
7. Jia, H.; Zheng, J.; Song, J.; Luo, L.; Yi, R.; Estevez, L.; Zhao, W.; Patel, R.; Li, X.; Zhang, J.-G., A novel approach to synthesize micrometer-sized porous silicon as a high performance anode for lithium-ion batteries. *Nano Energy* **2018,** *50*, 589-597.